

[rsc.li/esadvances](http://rsc.li/esadvances)

Justin Chaillot, <sup>\*a</sup> Sanjeev Dasari, <sup>b</sup> H  l  ne Fleurbaey,<sup>a</sup> Mathieu Daeron,<sup>c</sup>  
Jo  l Savarino<sup>b</sup> and Samir Kassi<sup>\*a</sup>

### Environmental significance

Sulfur isotope analyses are used in a variety of earth and environmental science domains. However, commonly used analytical techniques, *e.g.*, isotope ratio mass spectrometry, suffer from several issues such as mass interference, analytical requirements for a specially built conversion line and even hazardous nature of the potentially dangerous chemical procedure. These issues limit the operational capacity and analytical capabilities. As an alternative, we demonstrate a laser spectroscopy-based technique for simultaneous ultra-precise detection of triple-sulfur isotopes and a highly simplified sample preparation. The achieved precision represents a new benchmark for optical determination of isotopic measurements. This experimental set-up opens new frontiers for a wide range of applications from understanding the geochemistry and fractionation of sulfur isotopes to environmental sensing.

Sulfur (S) is one of the essential elements for life. The sulfur biogeochemical cycle links the atmosphere, biosphere, hydrosphere, and lithosphere.<sup>1</sup> Global S cycling involves the transformation of sulfur between several oxidation states  $-2$  (as in sulfide and reduced organic sulfur) to  $+6$  (as in sulfate). In addition, oxidation states of  $-2$  and  $0$  (as in elemental sulfur) are found in reduced inorganic forms of sulfur commonly in anoxic environments (*e.g.*, marine sediments). Other than these, sulfur species of mixed valence states (as in thiosulfate and polythionates) are also produced transiently.<sup>2</sup> These transformations play a vital role in both the assimilative and

dissimilative microbial functions, thereby sustaining biological processes as well as geological/mineralization processes.

The majority of natural and anthropogenic S is released directly as SO<sub>2</sub> (gas) or oxidized to SO<sub>2</sub> in the atmosphere.<sup>3</sup> Natural emissions of SO<sub>2</sub> (marine and volcanic) have been surpassed by anthropogenic emissions since the 1940s (fossil fuel burning *e.g.*, coal).<sup>3</sup> On a global scale,  $\approx 50\%$  of SO<sub>2</sub> is oxidized to sulfate while the rest is lost to dry and wet scavenging.<sup>4</sup> The pathway taken by SO<sub>2</sub> to form sulfate has major implications for both the radiative effect and the environment. In gas phase reactions, the end-product sulfuric acid gas leads to the formation of new particles eventually altering the albedo and lifetime of clouds.<sup>5</sup> This pathway can also lead to acid rain in the absence of neutralizing agents. Sulfate also acidifies particles, changing the bioavailability of many trace elements (*e.g.*, Fe) which are key to global biogeochemical cycles.<sup>6</sup> In heterogeneous phase reactions occurring primarily in clouds, sulfate particles contribute towards modifying the aerosol size distribution and cloud condensation nuclei activity.<sup>7</sup> These processes affect both direct and indirect aerosol radiative forcing. On a global scale, sulfate aerosols are found to be cooling in nature, thereby partially counterbalancing the effects

*“Laboratoire Interdisciplinaire de Physique (LIPhy), Université Grenoble Alpes, CNRS, Grenoble F-38000, France. E-mail: justin.chaillot@univ-grenoble-alpes.fr; samir.kassi@univ-grenoble-alpes.fr*

<sup>b</sup>*Institut des Géosciences de l'Environnement (IGE), Université Grenoble Alpes, CNRS, IRD, Grenoble INP, Grenoble F-38000, France*

*Laboratoire des Sciences du Climat et de l'Environnement (LSCE/IPSL), Université Paris-Saclay, CEA-CNRS-UVSQ, Gif-sur-Yvette F-91191, France*

of greenhouse gas warming. However, the magnitude and expected future changes in sulfate aerosol radiative forcing remain one of the largest uncertainties associated with assessments of climate change.<sup>8</sup> Addressing these uncertainties is one of the major challenges in atmospheric/earth sciences. To this end, S-isotope analysis, which historically has been limited to  $^{34}\text{S}/^{32}\text{S}$  but recently extended to  $^{33}\text{S}/^{32}\text{S}$  and  $^{36}\text{S}/^{32}\text{S}$  to access mass-independent fractionation (MIF)<sup>11–13</sup> [*i.e.*  $\Delta^{33}\text{S} = (\delta^{33}\text{S} + 1) - (\delta^{34}\text{S} + 1)^{0.515}$  and  $\Delta^{36}\text{S} = (\delta^{36}\text{S} + 1) - (\delta^{34}\text{S} + 1)^{1.889}$ ], provides powerful information for deconvolution of sources and atmospheric processes and has been applied in a wide range of studies, *e.g.*, pollution fingerprinting, chronicling the emergence of life by determining the period when atmospheric oxygen became abundant in the Earth's atmosphere.<sup>9–11</sup> The use of conventional isotope ratio mass spectrometry (IRMS) for measuring these S isotopes has posed several methodological and analytical limitations in terms of set-up, mass interference and throughput.<sup>12</sup> This is attributable to the fact that S isotopes on IRMS are usually analyzed as either  $\text{SO}_2$  or  $\text{SF}_6$ . While the former involves problems related to overlaps between  $^{33}\text{SO}_2$  and  $\text{S}^{17}\text{O}$  masses, the latter requires installation of an in-house conversion line and is also a potentially dangerous chemical conversion. In addition, other methods also exist which use the MC-ICP-MS for measurement of S-isotopes,<sup>13</sup> but measurement uncertainties can be an order of magnitude higher than what the IRMS method permits and, more importantly, the valuable  $^{36}\text{S}$  information is lost because of mass interference.<sup>13</sup> Both these methods also come with significant investment in terms of time and cost. It is therefore necessary to develop alternative methods for conducting more extensive measurements of S-isotopes.

### Spectroscopic methods

Absorption spectroscopy is an appealing alternative to conventional methods as it is not prone to isobaric interference. It relies on internal distribution of mass rather than the total mass of an isotopologue.<sup>14</sup> The spectroscopic approach relies on the fact that each isotopologue possesses its own and specific absorption spectrum, which consists of a series of narrow absorption features, so-called absorption lines with strength that vary over several orders of magnitude. Importantly, for a given temperature, the area of each single line is proportional to the partial pressure of the corresponding isotopologue. This practically compresses the instrumental dynamics needed to measure the relative abundance of the isotopologues. This is very different from mass spectrometry which deals with counting ions over a very broad dynamic range. Somehow, the choice of the strength of an absorption line plays the role of a signal gain knob. Interestingly, in some narrow spectral region that can be recorded using a single laser source, weak lines of the main isotopologue lie close to stronger ones of minor isotopologues. If the strength of each line is known – they are constant by nature – measuring the area of each absorption line permits determination of isotopic concentration and isotopic ratios. In practice, the strengths are not yet known with enough accuracy to determine the absolute isotopic concentration of gases; both theory and experiments are limited to a few per mil: the

former because of insufficient calculation power and model robustness, the latter because of the lack of pure samples despite the very high precision and accuracy optical spectroscopy offers.<sup>14</sup> Nevertheless, the variation of the isotopic ratio between two samples can be determined with high relative accuracy.

We have developed a new spectrometer dedicated to simultaneous multiple-S-isotope ( $^{32}\text{S}$ ,  $^{33}\text{S}$ ,  $^{34}\text{S}$ ) analysis based on near-infrared laser spectroscopy of hydrogen sulfide, *i.e.*,  $\text{H}_2\text{S}$ .  $\text{H}_2\text{S}$ , one of the key intermediates in the S biogeochemical cycle, has the advantage of being easily produced by sulfur reduction without the need for any specific chemical installation.<sup>2,12</sup> Furthermore, monitoring of  $\text{H}_2\text{S}$  in ambient air is crucial as exposure to trace levels of this gas has been known to be harmful for humans.<sup>15</sup>

So far, only a few studies have used spectroscopic methods for trace detection of  $\text{H}_2\text{S}$  concentration,<sup>16–21</sup> with a single study conducting S-isotope measurements.<sup>21</sup> These studies have led to generally poor detection limits and targeted  $\text{H}_2\text{S}$  transition lines lying around  $\approx 7\text{--}8\ \mu\text{m}$  ( $1428\text{--}1250\ \text{cm}^{-1}$ ) *i.e.*, in the mid-infrared spectral region.<sup>16–21</sup> In the present work, we explore a previously unexploited region of the  $\text{H}_2\text{S}$  spectra  $\approx 1.6\ \mu\text{m}$  ( $\approx 6250\ \text{cm}^{-1}$ ), which falls in the wavelength range commonly used for fibre optic transmissions, by taking advantage of a robust laser source and optical components, highly reflective mirrors, and sensitive photodetectors. Our system builds on previous work by Burkart *et al.* which offers unmatched laser frequency stability by employing a new kind of laser source obtained by optical feedback locking of a distributed feedback laser to an ultra-stable V-shaped optical cavity (VCOF).<sup>22,23</sup> Combining VCOF with the Cavity Ring-Down Spectroscopy (CRDS) technique, which provides a path length of several kilometres with 12 000 ring-downs per min, allows for a high temporal resolution and very high detectivity.<sup>24</sup> We report preliminary results on  $\text{H}_2\text{S}$  isotopic ratio anomaly determination in static and flow measurements, together with a precise spectroscopic study including line parameter pressure dependence in order to build an in-house data fitting procedure. To the best of our knowledge, these aspects have not been investigated in the literature related to S-isotopic spectral characterization of  $\text{H}_2\text{S}$ .<sup>21</sup> We also present a comparison with the international HITRAN database (<https://hitran.org/>),<sup>25</sup> which includes very few transitions of  $\text{H}_2\text{S}$  in the near-infrared spectral region. In summary, our spectrometer, which allows direct measurement of  $\text{H}_2\text{S}$  concentration and triple isotopic composition in a cost-effective spectral region, has a wide range of applications. These span from environmental detection of harmful pollutants to the identification and assessment of the impact of anthropogenic sulfur compounds, *e.g.*, on the biological cycle of sulfur and on the marine sediment cycle, as well as the impact of volcanic eruptions on the atmosphere.

## Materials and methods

### Experimental setup

The experimental set-up builds on two optical cavities: a first one dedicated to laser stabilization by external optical feedback (*i.e.*, a V-shaped cavity for optical feedback, VCOF) and a second



one being the measurement cavity (*i.e.*, a cavity ring down spectrometer, CRDS) filled with the gas under investigation (Fig. 1). The set-up, referred to as VCOF-CRDS, is discussed here in detail (all elements of the set-up are shown in Fig. 1).

### Laser frequency metrology

The laser source is a fibered distributed feedback laser, an easily available and widely used telecom technology. However, these lasers are noisy and have rather unstable emission frequency. They have a typical linewidth in the MHz range and frequency drifts of several tens of MHz that would highly limit the accuracy of measurements if not stabilized. With the optical feedback between the cavity and the laser, the emission spectra of the diode can be squeezed, and the stabilization of its central emission frequency can be achieved by transferring the robust optical stability properties of the cavity to the laser itself. In practice, the optical feedback mechanism reduces the laser linewidth well below 1 kHz while keeping its average emission frequency stabilized to better than  $10 \text{ Hz s}^{-1}$ . The emission

frequency of the VCOF source is determined using a wavemeter reading (High Finesse, 30 MHz resolution) refined to the kHz level using a frequency comb (Menlo Systems optical comb in Fig. 1). The VCOF source and comb tooth are mixed on a fast photodiode to record the frequency beat note equal to their optical frequency difference which lies between 0 and 125 MHz. The repetition rate (250 MHz) and carrier offset frequencies (20 MHz) of the comb are locked against a 10 MHz rubidium clock, itself disciplined to the GPS timing signal. This permits an absolute determination of the laser frequency and virtually, unlimited stability of the laser emission frequency. As such, we achieve unmatched precision in the measurements.

### Optical feedback (OF) mechanism

The OF mechanism occurs when photons from an external cavity excited by a laser come back into the laser gain medium. If the distance from the laser and the cavity is a multiple of half the emission wavelength, the back-propagating photons are in phase with the ones amplified inside the laser cavity. They are

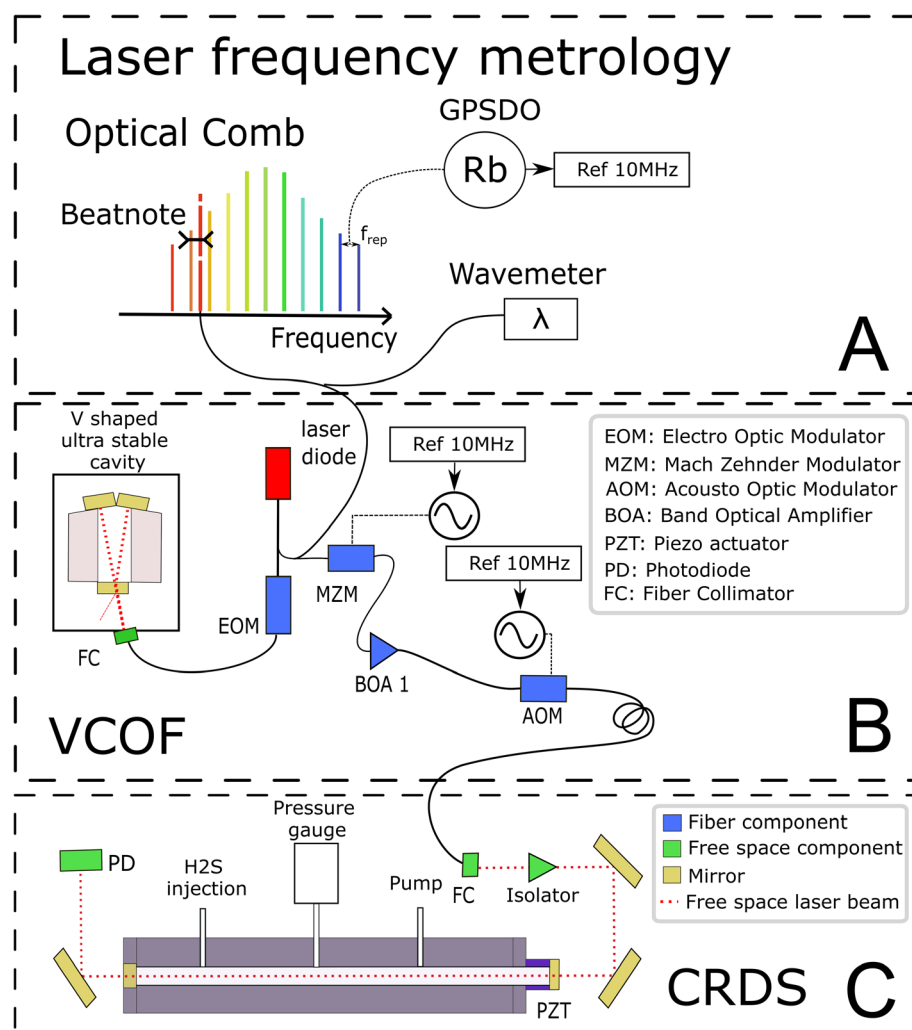


**Fig. 1** A schematic of the various components of the VCOF-CRDS system. The figure is structured in three blocks, detailing from top to bottom, (A) the frequency calibration, (B) the light source and (C) cavity ring-down spectrometer (CRDS), respectively. GPSDO stands for GPS disciplined oscillator, and VCOF stands for V-shaped cavity-based optical feedback.



therefore efficiently amplified in an avalanche and competitive manner what leads to an emission width well below the VCOF cavity mode width. In the present set-up, the phase is adjusted using an electro-optical phase modulator (EOM) (patent WO 2018/060285A1). This allows robust phase control using a PID controller with a bandwidth of a few tens of kHz. To provide intrinsic long term frequency stability – as desired for a potentially field deployed instrument – the VCOF is designed using thermally stable materials (Invar, ULE glass) and isolated from vibrations by an active optical table<sup>26–27</sup> The VCOF permits high stabilization of the laser, but spectroscopy requires an additional tuning scheme. The latter is provided by a Mach–Zehnder Modulator (MZM) used as an optical single-sideband modulator. It permits addition or subtraction of a radio frequency (RF) to the optical frequency in a very agile way.<sup>22</sup> The RF is provided by a microwave synthesizer tunable from 2 to 20 GHz. Because the MZM insertion losses are high (10 dB), the frequency shifted laser is further amplified using a Booster Optical Amplifier (BOA) before being injected into the CRDS. An optical isolator protects the BOA and the VCOF against photons that are reflected by the highly reflective mirrors of the CRDS. Tuning the RF permits recording of absorption spectra and dynamic compensation for the slow residual drift of VCOF, which in the lab is monitored at the kHz accuracy level as described above. The stability of the laser is crucial as it sets the reliability of the frequency axis over the measurement periods. The laser frequency must be stable to better than 10 kHz within this period, which is typically 3 seconds, to determine the line area with  $10^{-6}$  precision.

### Ring-down mechanism

A stable and tunable laser is injected into the CRDS cell using a single lens and two steering mirrors for a precise mode matching.<sup>22–24</sup> The stable CRDS optical cavity is made of a massive aluminium rod (70 mm outer diameter, 8 mm inner diameter, 490 mm length) with two high reflectivity mirrors fitted on its extremities (Layertec GmbH), one being mounted on a PZT actuator (PI) to finely adjust the cavity length to bring its modes in resonance with the probing laser. The cavity finesse  $F$  is in excess of 500 000 (mirror reflectivity  $> 0.99999$ ), providing very narrow optical modes and exceptional sensitivity ( $> 5 \times 10^{-13} \text{ cm}^{-1}$  routine detection limit).<sup>22–24</sup> Its free spectral range is 297 MHz and the photon lifetime is close to 300  $\mu\text{s}$ . The mean interaction path between the light and the gas is thus about 90 km. This is significantly higher in comparison to the  $\approx 4.2$  km path length in a previous spectroscopic study on  $\text{H}_2\text{S}$ .<sup>21</sup> The measurements are conducted following the continuous-wave-CRDS scheme.<sup>28</sup> In short, the laser is tuned and the cavity is brought into resonance with the laser. Photons that are passing through the mirror are essentially trapped in the cavity, leading to an increase of the intra-cavity power. The transmission of the cavity increases together with the number of photons circulating in the cavity. If the transmission exceeds a given threshold, the laser is interrupted using a fast acousto-optic modulator (AOM). The photons stored in the cavity then flush through the mirrors or vanish because of gas absorption. Both

effects result in an exponential decay of the transmission signal (ring-down event), whose time constant (ring-down time) is a reading of the mirror reflectivity and gas absorption contributions. The advantage of this technique is that it is immune to laser intensity fluctuations. Signal-to-noise ratios of up to  $10^6$  are reached in the present study by typically averaging 200 ring-down events over one second.

### Data acquisition

The reference gas sample used in this study is a mixture of 2000 ppmv  $\text{H}_2\text{S}$  in nitrogen at a total pressure of 150 bar (Air Liquide, Crystal 99.8%  $\text{N}_2$ , 2000 ppmv  $\text{H}_2\text{S}$ ). A regulator valve allows reducing gas pressure to the working pressure of 1 bar before it is injected into the instrument. The filling flow rate is controlled by a proportional solenoid valve (Bürkert Type 2871) with a 0.1 mm aperture. The evacuation rate is controlled using an additional solenoid valve. Pressure in the cavity is measured with a pressure gauge (Baratron AA01, 130 mbar range).

Temperature is expected to have a strong influence on the spectra of the sample ( $10^{-3} \text{ K}^{-1}$  on the isotopic ratios), because it affects the gas density and the line intensities. We took special care in providing a stable and homogeneous temperature in the CRDS cell. To ensure uniformity the cavity is made of aluminum. This material is a good thermal conductor which makes it possible to limit the temperature gradient. The cavity is as massive as possible to increase thermal time constants. It guarantees very low temperature excursions during the measurement of a spectrum. The cavity is placed in an isolated enclosure regulated by a commercial heat exchanger (Super-cool) at  $28^\circ\text{C}$  ( $\pm 0.05^\circ\text{C}$ ). A PT1000 probe is placed in a 20 mm deep hole drilled in the aluminum to regulate the cavity at  $29^\circ\text{C}$  with a heating wire wound around the cavity and controlled with a home-made PID regulator. Another PT1000, which is symmetrically placed, allows for additional temperature monitoring of the cavity. To limit the reaction of  $\text{H}_2\text{S}$  with walls and residual moisture, the tubing and cell have been treated with a protective coating (Silcotek Silconert™ 2000). The pressure regulators, the electro-valves, the CRDS PZT and the pressure gauge are not coated. A few Viton O-rings are in limited contact with the gas in the CRDS cell. The standard pressure inside the CRDS cell is 20 mbar for a volume of  $2 \times 10^{-5} \text{ m}^3$  corresponding to 33 nmol of  $\text{H}_2\text{S}$ . Each absorption spectrum was acquired by tuning the MZM from 2 to 20 GHz with a step resolution of 50 MHz to determine line parameters, but only a few spectral points are recorded for fast isotopic ratio determination.

The introduction of the gas sample can be done in two different modes. (1) Static: the cavity is repeatedly filled, the gas measured, and then evacuated. (2) Flow: using the pair of electro valves and the pressure gauge readings, a sample gas flow with regulated pressure is set to continuously regenerate the gas sample. Indeed, the reaction of  $\text{H}_2\text{S}$  in the CRDS cavity is clearly observed from the time dependence of the partial pressure retrieved from the absorption spectra, especially in static mode. In practice, an upper limit of 5 min per cycle of static measurements is found, after which the isotopic ratios are affected.





## Results

### S-isotope spectra and fitting regime

Before any potential application it is necessary to correctly characterize the absorption spectrum of the species studied. Therefore, we recorded a series of spectra for the  $\text{H}_2\text{S}$  reference gas at increasing total pressures from 17 to 23 mbar (Fig. 2). They were analyzed using the Multi-spectrum Analysis Tool for Spectroscopy (MATS)<sup>29</sup> developed at the National Institute of Standards and Technology (NIST). Each line (or group of lines in the case of the  $^{34}\text{S}$  doublet) was fit separately with a line profile that aims to reproduce the observed line shape as well as possible for all pressure values. Due to the high signal-to-noise ratio of the spectra, it was necessary to go beyond the Voigt profile – which includes both Doppler (Gaussian) broadening due to the thermal velocity of the molecules, and collisional (Lorentzian) broadening, as well as a collisional shift of the line position – to include more subtle collisional effects such as the Dicke narrowing (collisions modify the velocity distribution) and speed-dependence of the collisional broadening and shifting parameters. We have therefore selected the quadratic speed-dependent Nelkin–Ghatak profile (SDNGP)<sup>30</sup> in this work because it includes all these effects. The signal-to-noise ratio was however not sufficient to justify including a correlation between the two narrowing effects as in the Hartmann–Tran profile (HTP).<sup>31</sup>

The MATS program, written in the Python language, enables simultaneous fitting of several spectra recorded at different pressure conditions, imposing constraints on the pressure

dependence of line shape parameters. Here all fit parameters were set to be independent of pressure, except for the line intensities because the  $\text{H}_2\text{S}$  concentration in the cell was not accurately known due to degradation in the gas line as mentioned earlier. The line positions were fixed to the values retrieved from Lamb dip measurements as discussed below. The Doppler broadening was fixed to its calculated value. The fit residuals standard deviation is on the order of  $10^{-11} \text{ cm}^{-1}$  for the SDNGP fit and is two orders of magnitude smaller compared to the residuals from the HITRAN simulation (Fig. 2). Table 1 presents the obtained fit parameters for the four major lines in the region of interest.

The uncertainties in the intensities of the lines of the doublet ( $^{34}\text{S}_1$  and  $^{34}\text{S}_2$ ) are larger by an order of magnitude than those of the other lines. This is due to their overlap, which strongly correlates the two intensities. This translates into a total area of the doublet line that is better known (see fit residuals in Fig. 2) than each of its components. It should be noted that in the case of isotopic analysis based on optical spectroscopy methods, the line intensity does not have to be known with precision. Indeed, by definition of an isotopic ratio,<sup>32</sup> the isotopic measurements are relative to spectra realized on standard gases. The spectroscopic model is only there to compensate for the experimental variations (pressure, temperature) between the samples and the standards.

### Line position determination by Lamb dip measurement

The studied spectral zone is interesting because it contains the absorption lines of the three isotopologues of  $\text{H}_2\text{S}$  but one of

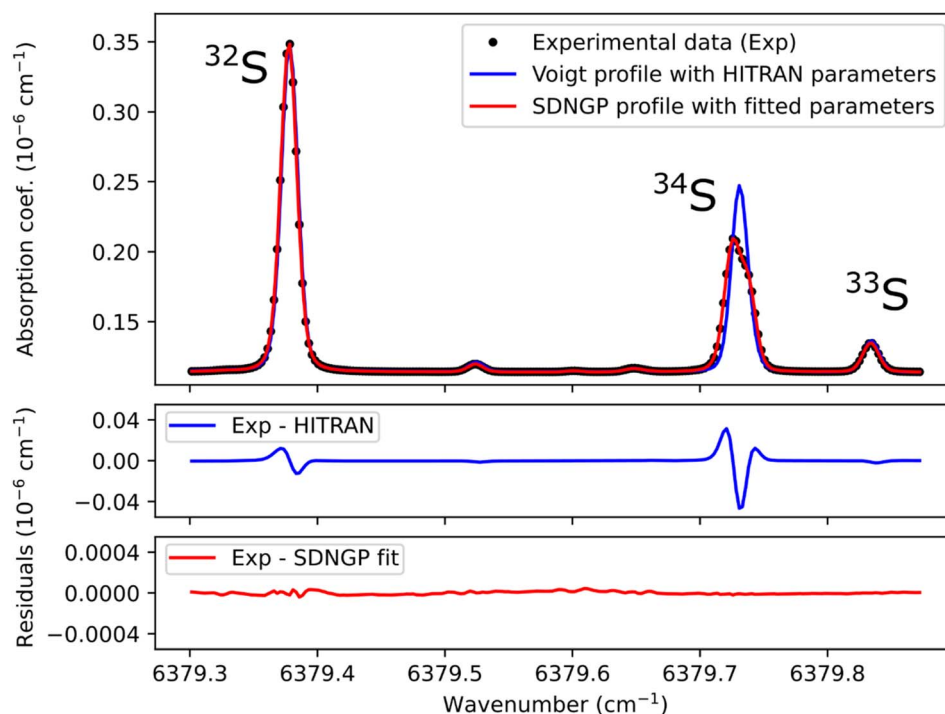


Fig. 2 This plot presents a spectrum recorded at a total pressure of 21 mbar (black dots), along with a Voigt profile simulation using HITRAN parameters (in blue) and a fit of the experimental values with the speed-dependent Nelkin–Ghatak profile (SDNGP, in red). The lower two panels show the difference between the experimental spectrum and each calculated curve. Note that the HITRAN positions were shifted by  $-0.003 \text{ cm}^{-1}$  for the simulation.



**Table 1** Fit parameters for the four most intense lines in the spectrum presented in Fig. 1. The SDNGP parameters and their units are shown in the table with the statistical fit uncertainty in the last digit in parentheses. The line intensity was fitted independently for different pressure values and is given here for the 21 mbar spectrum shown in Fig. 2, assuming an H<sub>2</sub>S mole fraction of 2000 ppm and natural isotopic abundance from HITRAN. The doublet <sup>34</sup>S peak fitting parameters are also shown

Isotope	<sup>32</sup> S	<sup>34</sup> S <sub>1</sub>	<sup>34</sup> S <sub>2</sub>	<sup>33</sup> S
Center frequency ( $\nu$ , cm <sup>-1</sup> )	6379.377777(2)	6379.725458(2)	6379.738104(3)	6379.834190(2)
Line intensity ( $S$ , 10 <sup>-25</sup> cm <sup>-1</sup> )	41.628(2)	15.38(1)	8.35(1)	3.4019(6)
Collisional broadening ( $\gamma$ , cm <sup>-1</sup> atm <sup>-1</sup> )	0.08224(2)	0.0888(2)	0.0480(3)	0.06895(8)
Shift ( $\delta$ , cm <sup>-1</sup> atm <sup>-1</sup> )	-0.009739(8)	-0.0082(3)	-0.0095(4)	-0.01150(3)
Rate of velocity-changing collisions ( $\nu_{vc}$ , cm <sup>-1</sup> atm <sup>-1</sup> )	0.0038(1)	0.0036(3)	0.0029(3)	0.0030(2)
Speed-dependence of broadening ( $a_w$ , dimensionless)	0.0658(6)	0.071(2)	0.128(5)	0.084(2)
Speed-dependence of shift ( $a_s$ , dimensionless)	0.083(1)	0.04(2)	-0.08(2)	0.023(2)

these lines is a doublet: it is composed of two lines very close to each other in frequency but coming from different energy levels of the molecule. The HITRAN database contains the two lines with different intensities but attributes the same frequency to

them. This approximation explains the difference between the simulated spectra and the experimental/measured spectra (Fig. 3A). To define the frequency of each one of the two lines, the Lamb dip measurement technique can be used (Fig. 3B).

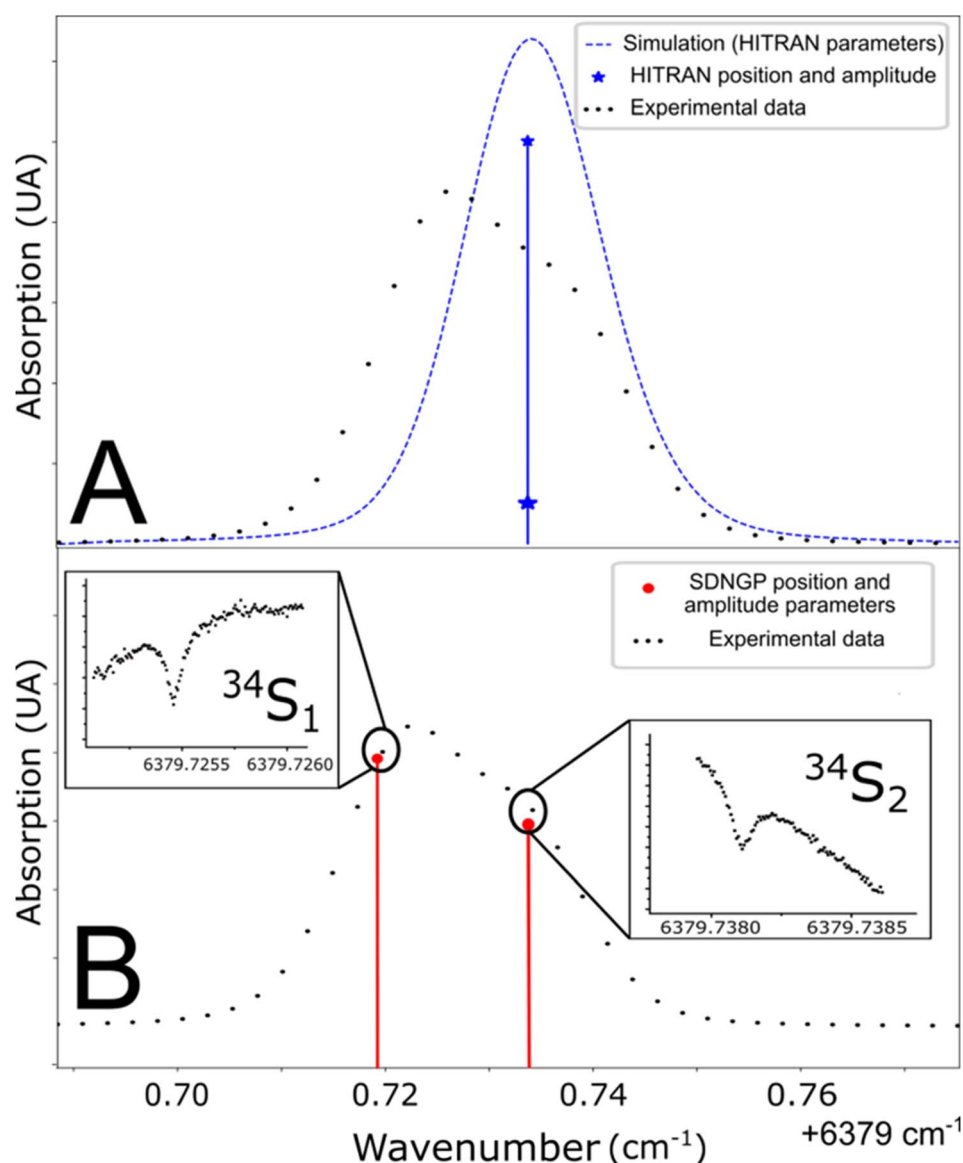


**Fig. 3** (A) Line position in the HITRAN database and simulation from these parameters (blue line). (B) Determination of doublet frequencies by Lamb dip measurement (red line).



Below, we provide more details of the characteristic Lamb dip feature.

In a molecule, the absorption of a photon of energy ( $h\nu$ ) occurs if it corresponds to the difference of two energy levels of the molecule  $E_2 - E_1$ , with  $E_2 > E_1$ . At room temperature, around 1.5  $\mu\text{m}$ , the higher energy level is unpopulated. Even if a photon is absorbed, the higher-level population remains negligible. This is particularly true in the presence of molecular collisions which actively participate in the higher-level depopulation. But at very low pressure and high photon fluxes, this approximation is no more valid, and the absorption seems lowered because of the competition between absorption from the lower state and stimulated emission from the higher state. The transition enters a so-called saturation regime. In an extreme situation the population can be equally shared between lower and higher levels and the medium then appears transparent. The signature of saturation is an optical power dependence of the absorption.

Interestingly, in an optical cavity, photons are traveling back and forth through the gas, which has a temperature related Gaussian velocity distribution of its molecules that is responsible for the Gaussian line shape of the molecular absorption (as in Fig. 2). It is wide by about 600 MHz. Obviously, molecules that have no velocity component along the cavity axis absorb resonant photons traveling on both sides. In contrast, molecules moving along the axis encounter two different frequencies because of the Doppler effect due to their movement. They can only absorb photons traveling from a single direction. In the presence of saturation, molecules with no velocity along the axis are therefore twice as saturated as the others. This manifests as a narrow absorption dip in the exact middle of the absorption line, whose width is essentially due to the time of flight through the cavity mode beam, residual collisions, and power broadening effect. This regime can be achieved in the VCOF-CRDS system at low pressure, and for strong absorption, thanks to the five orders of magnitude power enhancement brought by the high finesse resonant cavity.

Fig. 3 shows spectra recorded in such a regime, at a pressure of 0.1 mbar. The laser frequency was roughly stepped (50 MHz step) to reveal the broad Gaussian shape of the line and then finely stepped (50 kHz) close to the center of the absorption line. The Lamb dip feature is well marked. It indicates the zero-pressure position of the line with high precision and accuracy. This is the first report of the Lamb dip feature for S-isotope spectra of  $\text{H}_2\text{S}$ . We repeated the measurement for the three isotopologues to determine every absorption frequency. It is worth noting that this permits unambiguous determination of individual positions for the blended  $\text{H}_2^{34}\text{S}$  doublet (as seen in Fig. 3). The obtained positions were used to constrain the multi-pressure fit (Table 1). We insist that no saturation effect was observed above 1 mbar.

### Estimation of measurement precision

The high-resolution spectra recorded to conduct the pressure dependent fit have a necessarily limited accuracy and precision. To be properly determined, the uncertainties of the fitted parameters must consider the fluctuations of the external

physical parameters and their own uncertainties. Following BIPM recommendations for such an approach,<sup>32</sup> we proceed as follows: let us consider the measured absorption spectrum to be a function  $Y$  which depends on four different parameters, namely the temperature  $T$ , the pressure  $P$ , the frequency  $f$  and the absorption of the gas  $\alpha$ . This set of parameters forms the vector  $B$ . If the function  $Y$  produced by the spectroscopic model is realistic – *i.e.*, leading to essentially flat and limited residuals – the Jacobian vector  $J$  and the covariance matrix permit a reliable evaluation of the uncertainties. The Jacobian vector reads

$$J = \begin{pmatrix} \frac{\partial Y}{\partial f} \\ \frac{\partial Y}{\partial T} \\ \frac{\partial Y}{\partial P} \\ \frac{\partial Y}{\partial \alpha} \end{pmatrix} \quad (1)$$

The covariance matrix  $\text{cov}(B)$  can then be written as follows and simplified by setting uncorrelated parameters to 0:

$$\begin{aligned} \text{cov}(B) &= \begin{pmatrix} \text{cov}(T, T) & \text{cov}(T, P) & \text{cov}(T, f) & \text{cov}(T, \alpha) \\ \text{cov}(P, T) & \text{cov}(P, P) & \text{cov}(P, f) & \text{cov}(P, \alpha) \\ \text{cov}(f, T) & \text{cov}(f, P) & \text{cov}(f, f) & \text{cov}(f, \alpha) \\ \text{cov}(\alpha, T) & \text{cov}(\alpha, P) & \text{cov}(\alpha, f) & \text{cov}(\alpha, \alpha) \end{pmatrix} \\ &= \begin{pmatrix} \sigma^2(T) & \text{cov}(T, P) & 0 & 0 \\ \text{cov}(P, T) & \sigma^2(P) & 0 & 0 \\ 0 & 0 & \sigma^2(f) & 0 \\ 0 & 0 & 0 & \sigma^2(\alpha) \end{pmatrix} \end{aligned} \quad (2)$$

Finally, the uncertainty  $\sigma^2(Y(\nu))$  reads:

$$\sigma^2(Y(\nu)) = \text{cov}(Y(\nu), Y(\nu)) = J \text{cov}(B) J^t \quad (3)$$

From this experimental uncertainty we can estimate the uncertainty in isotopic ratio measurements. This theoretical experimental uncertainty is compared to the statistics carried out on a corpus of 1000 spectra. A good agreement is observed between the calculated  $\sigma^2$  value and the thickness of the trace of isotopic ratios, but this study highlights a drift in measurements. Measurement strategies need to be put in place to correct these drifts. The standard solution is the alternative use of sample and standard injections using a gas management system.

## Discussion

The spectroscopic investigation of  $\text{H}_2\text{S}$  isotopologues in the near-infrared region was conducted from a high- to low-pressure regime (21 mbar and 0.1 mbar) with the so-called VCOF-CRDS setup. Spectroscopic parameters of  $\text{H}_2\text{S}$



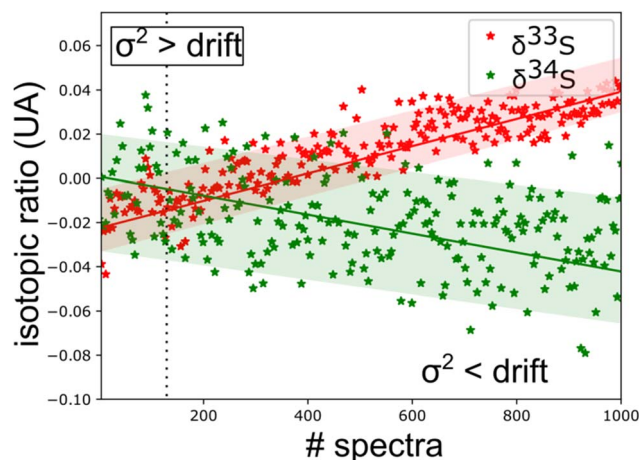


Fig. 4 Time series of isotopic ratio measurements (3 s per spectra) reveal a spectral interference between  $\text{H}_2\text{S}$  and other outgassed molecules [ $\text{CO}_2$  lines are observed in 'old' gas (Fig. 5)]. This sets a limit to the experimental repeatability.

absorption lines and their pressure dependence were assessed with a multi-pressure fit and their uncertainties were determined. A drift was evidenced in the measurement of isotope ratios (Fig. 4). Plausible explanations for this drift are as follows: (a) an issue with the temperature/pressure sensor that affects the gas absorption lines, (b) a thermo-mechanical stress that affects the optical alignment, which slowly distorts the baseline, (c) spectral interference by outgassing molecules like the above-mentioned  $\text{CO}_2$  lines overlapping with the  $^{34}\text{S}$  line, as shown in Fig. 5. Monitoring the isolated strong line of  $\text{CO}_2$  permitted explicit addition of  $\text{CO}_2$  contribution in the spectroscopic fitting model. Interestingly, water vapor was never detected over the

entire experiment period even though it is known to continuously outgas even with a dedicated cell coating. We suspect it is chemically destroyed by reaction with  $\text{H}_2\text{S}$ , what may partly also explain the short lifetime of  $\text{H}_2\text{S}$  in the cell. We estimate that the isotopic ratio drift is most likely due to the spectral interference from other gas molecules. Further investigations are planned to better understand the pattern of the drift.

We conclude that a precision (repeatability) of 5 ppm can be achieved for up to 10 spectral measurements within less than 1 minute. This high precision makes it possible to perform isotopic ratio measurements on  $\text{H}_2\text{S}$  for real world applications. However, to understand the accuracy (reproducibility) of the system a simultaneous injection of the 'sample' and 'standard' of known isotopic composition is needed. This can be achieved with an efficient gas management system *i.e.*, a dual-inlet system, which is under construction. This aspect will be explored as part of future study with the VCOF-CRDS setup. Moreover, we are planning to investigate the less abundant  $\text{H}_2^{36}\text{S}$  isotope spectrum, whose spectrum is unknown in this region.

Summing up, the VCOF-CRDS system opens new frontiers in laser spectroscopy-based isotope measurements of  $\text{H}_2\text{S}$ . The robustness of the system in terms of the ultrahigh sensitive laser linewidth (a few kHz) coupled to a huge optical pathlength allows for high-precision measurements. The detection of the Lamb dip features of the triple S-isotopes confirms the laser quality and instrumental sensitivity and permitted high refinement of  $\text{H}_2\text{S}$  line positions. The spectral fitting approach developed in this study can be extended to further investigations of  $\text{H}_2\text{S}$  in the near IR region and the present line parameters of  $^{34}\text{S}$ ,  $^{33}\text{S}$  and  $^{32}\text{S}$  lines complement the HITRAN database, which is very sparse in this region. This analytical instrument paves the way for a wide range of applications in the fields of sulfur isotope geochemistry, biomedical applications and environmental sensing.

## Author contributions

S. K., J. S., M. D. and J. C. built the instrument; J. C., S. K. and S. D. conducted the measurements; H. F. and J. C. performed the pressure-dependent spectral fit; S. D., J. C. and S. K. drafted the paper and wrote the paper with input from all co-authors.

## Conflicts of interest

The authors declare no competing financial interests.

## Acknowledgements

S. D. and J. S. acknowledge support from the Marie Skłodowska-Curie Action grant number 1010180 (to S. D.; hosted by J. S.). S. K. and J. S. acknowledge financial support from the French National program LEFE (Les Enveloppes Fluides et l'Environnement), the MITI initiative "Défi Isotope" of the CNRS and the LabEx OSUG@2020 ("Investissements d'avenir" – ANR10 LABX56).

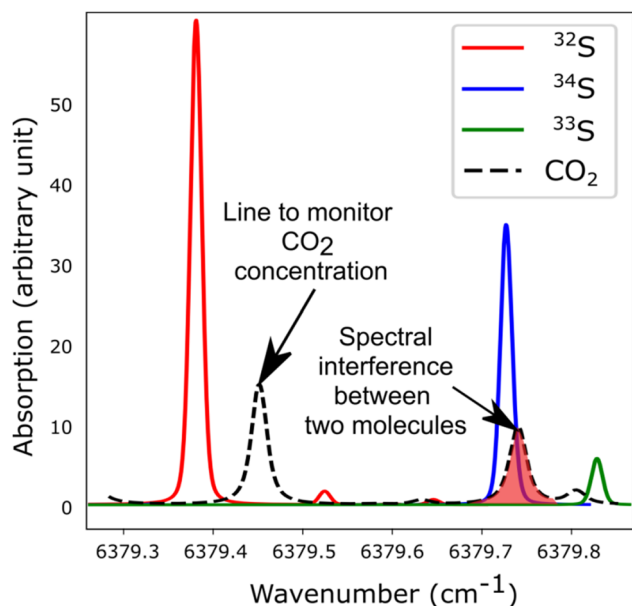


Fig. 5 Simulated spectra showing the S-isotopologue lines of  $\text{H}_2\text{S}$  and interfering  $\text{CO}_2$  lines in the spectral region covered by the VCOF-CRDS setup.





## References

- 1 H. G. Thode, *Sulfur isotopes in nature and the environment: an overview*, Wiley, England, 1991, vol. 43, pp. 1–26.
- 2 B. B. Jørgensen, A. J. Findlay and A. Pellerin, *Front. Microbiol.*, 2019, **10**, 849.
- 3 J. H. Seinfeld and S. N. Pandis, *Atmos. Chem. Phys.: From Air Pollution to Climate Change*, John Wiley & Sons, Inc., New York, 1996.
- 4 S. Solomon et al., *Climate Change 2007: The Physical Science Basis, Contribution of the Working Group I to the Fourth Assessment Report of the Intergovernmental Panel on Climate Change*, Cambridge University Press, New York, 2007.
- 5 M. Kulmala and et al., *Science*, 2007, **318**, 89–92.
- 6 W. Li, X. Liang, X. Liu, J. Zhang, Y. Lin, X. Yao, H. Gao, D. Zhang, J. Chen, W. Wang and R. M. Harrison, *Sci. Adv.*, 2017, **3**, e1601749.
- 7 S. Mertes, D. Galgon, K. Schwirn, A. Nowak, K. Lehmann, A. Massling, A. Wiedensohler and W. Wiedensohler, *Atmos. Environ.*, 2005, **39**, 4233–4245.
- 8 P. Arias, et al., *Climate Change 2021: The Physical Science Basis. Contribution of Working Group I to the Sixth Assessment Report of the Intergovernmental Panel on Climate Change*, Cambridge University Press, New York, 2021.
- 9 J. O. Nriagu, R. D. Coker and L. A. Barrie, *Nature*, 1991, **349**, 142–145.
- 10 Y. Shen, R. Buick and D. E. Canfield, *Nature*, 2001, **410**, 77–81.
- 11 J. Farquhar, H. Bao and M. Thieme, *Science*, 2000, **289**, 756–759.
- 12 D. Yang, P. Cartigny, K. Desboeufs and D. Widory, *Atmos. Chem. Phys.*, 2019, **19**, 3779–3796.
- 13 G. Paris, A. L. Sessions, A. V. Subhas and J. F. Adkins, *Chem. Geol.*, 2013, **345**, 50–61.
- 14 J. Morville, D. Romanini and E. Kerstel, Cavity enhanced absorption spectroscopy with optical feedback, in *Cavity-Enhanced Spectroscopy and Sensing*, ed. G. Gagliardi and H.-P. Loock, Springer, Berlin Heidelberg, 2014, pp. 163–209.
- 15 G. D. Banik, A. De, S. Som, S. Jana, S. B. Daschakraborty, S. Chaudhuri and M. Pradhan, *J. Breath Res.*, 2016, **10**, 026010.
- 16 H. Moser, W. Pölz, J. P. Wacławek, J. Ofner and B. Lendl, *Anal. Bioanal. Chem.*, 2017, **409**, 729–739.
- 17 M. Nikodem, K. Krzempek, D. Stachowiak and G. Wysocki, *Opt. Eng.*, 2017, **57**, 011019.
- 18 M. S. De Cumis, S. Viciani, S. Borri, P. Patimisco, A. Sampaolo, G. Scamarcio, P. De Natale, F. D'Amato and V. Spagnolo, *Opt. Express*, 2014, **22**, 28222.
- 19 M. Helman, H. Moser, A. Dudkowiak and B. Lendl, *Appl. Phys. B*, 2017, **123**, 1–8.
- 20 H. Moser, A. Genner, J. Ofner, C. Schwarzer, G. Strasser and B. Lendl, *Opt. Express*, 2016, **24**, 6572.
- 21 M. Pal, M. S. Maithani, A. Maity and M. Pradhan, *J. Anal. At. Spectrom.*, 2019, **34**, 860–866.
- 22 J. Burkart, D. Romanini and S. Kass, *Opt. Lett.*, 2013, **38**, 2062–2064.
- 23 J. Burkart, D. Romanini and S. Kass, *Opt. Lett.*, 2014, **39**, 4695–4698.
- 24 T. Stoltmann, M. Casado, M. Daeron, A. Landais and S. Kass, *Anal. Chem.*, 2013, **89**, 10129–10132.
- 25 I. E. Gordon and et al., *J. Quant. Spectrosc. Radiat. Transfer*, 2022, **277**, 10794.
- 26 M. Casado, T. Stoltmann, A. Landais, N. Jobert, M. Daëron, F. Prié and S. Kass, *Appl. Phys. B: Lasers Opt.*, 2022, **128**, 1–7.
- 27 N. Jobert, M. Casado and S. Kass, *Appl. Phys. B: Lasers Opt.*, 2022, **128**, 1–7.
- 28 D. Romanini, P. Dupré and R. Jost, *Vib. Spectrosc.*, 1999, **19**, 93–106.
- 29 E. M. Adkins, *Multi-Spectrum Analysis Tool for Spectroscopy*, 2020, DOI: [10.18434/M32200](https://doi.org/10.18434/M32200).
- 30 H. Tran, N. H. Ngo and J. M. Hartmann, *J. Quant. Spectrosc. Radiat. Transfer*, 2013, **129**, 199–203.
- 31 N. H. Ngo, D. Lisak, H. Tran and J. M. Hartmann, *J. Quant. Spectrosc. Radiat. Transfer*, 2013, **129**, 89–100.
- 32 Joint Committee for Guides in Metrology, *Guide to the Expression of Uncertainty in Measurement*, Paris, 2008.

